




# Primordial Earth Mantle Heterogeneity Caused by the Moon-forming Giant Impact?

Hongping Deng<sup>1</sup> , Maxim D. Ballmer<sup>2</sup>, Christian Reinhardt<sup>1</sup>, Matthias M. M. Meier<sup>3</sup>, Lucio Mayer<sup>1</sup>, Joachim Stadel<sup>1</sup>, and Federico Benitez<sup>1</sup>

<sup>1</sup> Center for Theoretical Astrophysics and Cosmology, Institute for Computational Science, University of Zurich, Winterthurerstrasse 190, 8057 Zurich, Switzerland  
[hpdeng@physik.uzh.ch](mailto:hpdeng@physik.uzh.ch)

<sup>2</sup> Institute of Geophysics, ETH Zurich, Sonneggstrasse 5, 8092 Zurich, Switzerland

<sup>3</sup> Institute of Geochemistry and Petrology, ETH Zurich, Clausiusstrasse 25, 8092 Zurich, Switzerland

Received 2019 June 26; revised 2019 October 17; accepted 2019 October 22; published 2019 December 19

## Abstract

The giant impact hypothesis for Moon formation successfully explains the dynamic properties of the Earth–Moon system but remains challenged by the similarity of isotopic fingerprints of the terrestrial and lunar mantles. Moreover, recent geochemical evidence suggests that the Earth’s mantle preserves ancient (or “primordial”) heterogeneity that pre-dates the Moon-forming giant impact. Using a new hydrodynamical method, we here show that Moon-forming giant impacts lead to a stratified starting condition for the evolution of the terrestrial mantle. The upper layer of the Earth is compositionally similar to the disk, out of which the Moon evolves, whereas the lower layer preserves proto-Earth characteristics. As long as this predicted compositional stratification can at least partially be preserved over the subsequent billions of years of Earth mantle convection, a compositional similarity between the Moon and the accessible Earth’s mantle is a natural outcome of realistic and high-probability Moon-forming impact scenarios. The preservation of primordial heterogeneity in the modern Earth not only reconciles geochemical constraints but is also consistent with recent geophysical observations. Furthermore, for significant preservation of a proto-Earth reservoir, the bulk major-element composition of the Earth–Moon system may be systematically shifted toward chondritic values.

*Unified Astronomy Thesaurus concepts:* [Earth \(planet\) \(439\)](#); [Earth-moon system \(436\)](#); [Lunar composition \(948\)](#); [Satellite formation \(1425\)](#); [Computational methods \(1965\)](#)

## 1. Introduction

The Earth is orbited by a single and massive moon. The leading theory for the formation of the Earth–Moon system with its high angular momentum involves a giant impact followed by lunar aggregation from the impact debris disk (Hartmann & Davis 1975; Cameron & Ward 1976). The canonical giant impact model involves a graze-and-merge impact, in which a Mars-sized body (or “Theia”) collides with the proto-Earth at an oblique angle at roughly the escape velocity of the system (Canup & Asphaug 2001). However, smoothed particle hydrodynamics (SPH) simulations show Theia contributes a larger fraction of silicates ( $\sim 70\%$  by mass) to the proto-lunar disk than to the proto-Earth (Canup et al. 2013). Unless Theia and the proto-Earth had almost the same isotopic composition, this imbalance is at odds with the strong isotopic similarity of the Earth’s and lunar mantles, e.g., in terms of oxygen (Herwartz et al. 2014) and titanium (Zhang et al. 2012).

One way to reconcile this compositional similarity involves the post-impact re-equilibration of the Earth and the Moon-forming disk (Pahlevan & Stevenson 2007). The degree to which this model can produce Earth–Moon homogeneity depends on the depth of magma-ocean convection during the lifetime of the proto-lunar disk, which could limit equilibration to involve only the upper portions of the silicate Earth (Section 5 and Nakajima & Stevenson 2015). A near equal-mass “sub-Earth” impact (Canup 2012) or the disruption of a fast-spinning Earth (close to self-breakup) by a small impactor (Ćuk & Stewart 2012) can indeed explain the isotopic similarity. However, the proposed solutions are low-probability events; equal-mass collisions are highly unlikely in the late stage of planetary accretion (Mastrobuono-Battisti & Perets 2017), and

planetary embryos hardly reach spins that are close to self-breakup in hydrodynamic simulations (Rufu et al. 2017). Both models also predict an angular momentum that is too high for the early Earth–Moon system, and the mechanisms proposed to remove the excess angular momentum exclusively work in a narrow tidal parameter range (Wisdom & Tian 2015). Alternatively, multiple-impact models have been suggested for lunar origin (Rufu et al. 2017), certainly broadening the favorable parameter space compared to single-impact models, and giving rise to mixing through mergers of moonlets with different isotopic composition. However, the dynamics of moonlets are highly uncertain, and primitive moonlets might be lost during repeated impacts pre-dating the Moon-forming stage (Pahlevan & Morbidelli 2015). Lock et al. (2018) suggest the Moon forms within synestia (Lock & Stewart 2017), a post-impact structure of high-energy, high angular-momentum impact so that chemical equilibrium is naturally achieved during the condensation of the Moon. Covered with a thick magma ocean, the canonical impact model can also derive enough amount of target material in the proto-lunar disk to explain the isotopic similarity (Karato 2014; Hosono et al. 2019). However, the hard sphere EOS for the magma ocean in Hosono et al. (2019) may be oversimplified (R. Caracas, private communication).

Here, we explore the mixing state of the Earth–Moon system in low-velocity, low-angular-momentum impact scenarios. We consider the canonical model (Canup & Asphaug 2001) and the hit-and-run model (Reufer et al. 2012;  $v_{\text{imp}} < 1.3v_{\text{esc}}$ , where  $v_{\text{imp}}$  is the impact velocity and  $v_{\text{esc}}$  is the escape speed), which are both high-probability impact configurations (Jackson et al. 2017). We describe some general constraints due to angular momentum transport on material distribution in Section 2. We present impact simulations with the meshless finite mass

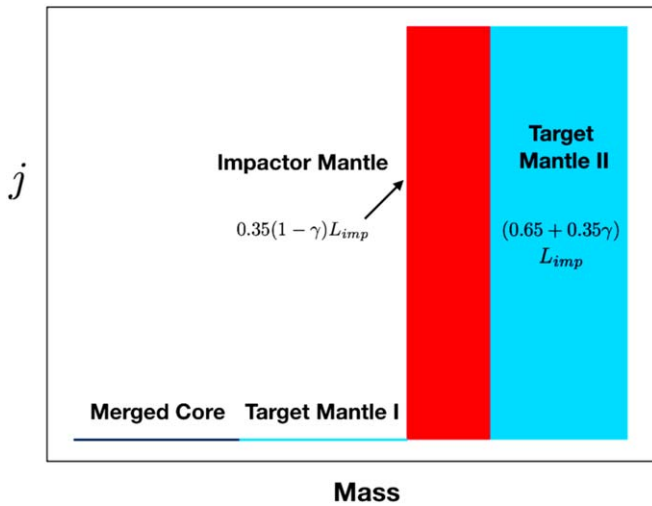


**Figure 1.** An idealized model to estimate the maximum possible penetration depth of impactor’s silicates in the post-impact target. The figure shows the specific angular momentum ( $j$ ), which must not decrease with radius to avoid rotational instability, of different components of the target and impactor; note the masses of different components are not drawn to scale. The target’s silicates that can be placed outside the impactor’s silicates are less than those lying inside the impactor’s silicates, thus the impactor’s silicates cannot penetrate half the target mantle for an impact with  $\gamma < 0.15$ .

(MFM) method (Hopkins 2015; Deng et al. 2019b) in Section 3. The geochemistry and geophysical implications of our simulation results are discussed in Sections 4 and 5. We remark on some numeric issues and the robustness of the model in Section 6. Finally, we conclude in Section 7.

## 2. Unavoidable Layering During the Impact

In the gravity dominated regime, the interaction between the impactor’s mantle and the target’s mantle behaves like a fluid collision. One fluid element can only deliver half its momentum/angular momentum to a roughly equal-mass fluid element due to the completely inelastic nature of a fluid collision. The transport of angular momentum through shock waves, primarily the contact shock at their first contact, is also inefficient because the shock is almost symmetric to the line of centers. The impactor’s mantle has an initial angular momentum of  $0.7(1 - \gamma)L_{imp}$ , where  $\gamma$  is the impactor to target mass ratio. It tends to lose about half its initial angular momentum (confirmed by our simulations), so that it cannot sink deep into the target’s mantle. To avoid centrifugal instability, the specific angular momentum of the post-impact target must not decrease as radius increases (Rayleigh Criterion); in simulations, the outer part rotates faster. Considering an idealized model where the impactor’s silicates penetrate deepest, the impactor’s silicates concentrate in a thin shell and they rotate with materials from the target’s mantle, residing outside the shell, at constant specific angular momentum (see Figure 1). The materials beyond the shell contain the rest of the angular momentum,  $(0.65 + 0.35\gamma)L_{imp}$ . Even for  $\gamma = 0.15$ , the impactor’s mantle cannot penetrate half the target’s mantle. A hit-and-run collision is more complicated due to interaction with the escaping part and stronger oblique shocks, but the angular momentum transport is still inefficient (see Table 1).

## 3. Simulations and Analysis

We simulate the giant impacts using the GIZMO code (Hopkins 2015), which is a descendant of the GADGET code (Springel 2005) and its SPH method widely used in previous impact simulations. GIZMO indeed contains the legacy SPH implementation of the GADGET code, newer SPH implementations such as density independent SPH, and, most importantly, the novel MFM.<sup>4</sup> Gravity is coupled to all these different hydro methods using the same treecode scheme (Hopkins 2015). The MFM method is an improved hydrodynamics formulation that is fundamentally different from the SPH. GIZMO MFM does effective volume partition according to the particle distribution and then solves the Riemann problem to update the fluid variables and can be regarded as a generalized moving mesh method. It employs no explicit artificial viscosity (see e.g., Springel 2005) and thus shows better conservation property than SPH (Deng et al. 2017). MFM captures shocks and subsonic turbulence in giant impact simulations accurately, so it can simulate the mixing properly (Deng et al. 2019b). We use about 500 K particles in our simulations, which is comparable to present-day high-resolution simulations. There are some discussions about numerical convergence of SPH simulations of giant impacts using more than  $10^8$  particles (Hosono et al. 2017; Kegerreis et al. 2019). We note MFM has a different convergence rate (see, e.g., Deng et al. 2019a) from SPHs, which is limited by the typically fixed number of neighbors as well (Zhu et al. 2015). Preliminary convergence test for MFM is presented in Section 6.2 and dedicated study is desirable in the future.

We apply the ANEOS/M-ANEOS equation of state (Thompson & Lauson 1974; Melosh 2007) with iron comprising the core and dunite comprising the mantle. We build the initial condition for planets (30 wt% iron, 70 wt% dunite) by solving the hydrodynamic equilibrium with an isentropic profile and place the particles (computational elements) in spherical shells to represent the equilibrium profile (Reinhardt & Stadel 2017). The temperature on the planet surface is about 2000 K, corresponding to an entropy of  $2700 \text{ J kg}^{-1} \text{ K}^{-1}$  in the mantle and  $1200 \text{ J kg}^{-1} \text{ K}^{-1}$  in the core. We run a comparison study with higher initial entropy and our results are robust concerning the initial entropy value (see Section 6.2).

In our simulations of such impacts, a strong shock propagates almost perpendicular to the line connecting the centers of the two impacting bodies after the first contact. In both the canonical and hit-and-run scenarios, the part of the impactor that can avoid direct collision is sheared into a spiral structure that, shortly afterwards, collapses into clumps. The clumps reimpact the highly distorted target to eject some additional target material into the circumplanetary debris disk (Figure 3(b)).<sup>5</sup> We characterize the modeled impacts by determining the disk mass and angular momentum, the predicted Moon mass, planet mass/angular momentum and the internal structure of the post-impact target. The former is done following a standard approach, i.e., bounded particles with periapsis distance larger than the equatorial radius of the planet are classified as disk particles (Canup et al. 2013; Rufu et al. 2017). This calculation is performed at least 40 hr after the impact, i.e., when the system saturates to a quasi-steady

<sup>4</sup> The GIZMO code with Tillotson EOS is publicly available at <http://www.tapir.caltech.edu/~phopkins/Site/GIZMO.html>.

<sup>5</sup> Here is a movie showing the material distribution in run 13 ([https://drive.google.com/file/d/1pZQC3aX\\_wgDiwLhTi-XUKG3Z07lbsISR/view?usp=sharing](https://drive.google.com/file/d/1pZQC3aX_wgDiwLhTi-XUKG3Z07lbsISR/view?usp=sharing)).

**Table 1**  
Parameters and Results of Impact Simulations

Run	$\frac{M_{\text{tar}}}{M_E}$	$\frac{M_{\text{imp}}}{M_E}$	$b$	$\frac{v_{\text{imp}}}{v_{\text{esc}}}$	$\frac{L_F}{L_{EM}}$	$\frac{L_D}{L_{EM}}$	$\frac{M_D}{M_L}$	$\frac{M_{\text{planet}}}{M_E}$	$\frac{M_U}{M_{\text{mantle}}}$	$F_{U,\text{tar}}$	$F_{D,\text{tar}}$	$\frac{M_{\text{Fe}}}{M_D}$	$\frac{M_M}{M_L}$
1	0.85	0.12	0.71	1.00	0.91	0.16	0.87	0.94	0.46	0.84	0.38	0.16	0.73
2	0.85	0.12	0.73	1.00	1.18	0.35	1.48	0.95	0.50	0.86	0.40	0.04	1.48
3	0.85	0.16	0.71	1.00	1.30	0.32	1.70	0.98	0.49	0.80	0.30	0.04	1.5
4	0.85	0.16	0.73	1.00	1.30	0.23	1.22	0.98	0.43	0.79	0.39	0.12	1.08
5	0.90	0.16	0.71	1.00	1.32	0.32	1.98	1.0	0.52	0.81	0.47	0.01	1.19
6	0.90	0.16	0.73	1.00	1.53	0.38	1.64	1.0	0.52	0.80	0.34	0.05	1.64
7	0.85	0.2	0.574	1.20	1.33	0.29	1.63	0.99	0.59	0.79	0.52	0.08	1.26
8	0.85	0.2	0.574	1.25	1.26	0.26	1.45	0.98	0.62	0.80	0.47	0.09	1.14
9	0.90	0.2	0.537	1.20	1.30	0.05	0.30	1.06	0.55	0.79	0.64	0.01	0.20
10	0.90	0.2	0.537	1.25	1.32	0.13	0.81	1.04	0.60	0.79	0.62	0.03	0.48
11	0.90	0.2	0.537	1.30	1.30	0.20	1.20	1.04	0.54	0.79	0.55	0.12	0.79
12	0.90	0.2	0.574	1.15	1.38	0.14	0.88	1.04	0.54	0.79	0.59	0.01	0.51
13	0.90	0.2	0.574	1.20	1.34	0.23	1.23	1.02	0.56	0.79	0.57	0.08	1.07
14	0.90	0.2	0.574	1.25	1.30	0.24	1.30	1.02	0.59	0.80	0.54	0.09	1.30
15	0.90	0.2	0.574	1.30	1.20	0.23	1.18	1.02	0.50	0.79	0.44	0.16	1.18

**Note.** At the end of each run (at least 40 hr after the impact, until no clumps present in the disk) we evaluate the proto-lunar disk and the post-impact target compositions following an established approach (Canup et al. 2013; Rufu et al. 2017).  $M_E$ ,  $M_L$ ,  $M_D$ ,  $M_M$ ,  $M_{\text{planet}}$  are the real masses of the Earth and Moon, and the predicted masses of the proto-lunar disk, the formed moon, and post-impact target (formed Earth), respectively.  $L_F$ ,  $L_D$ ,  $L_{EM}$  are the angular momentum of the final bound system, proto-lunar disk, and the Earth–Moon system. We also calculated the mass fraction of the mantle that lies beyond  $R$ , i.e.,  $\frac{M_U}{M_{\text{mantle}}}$ . The fraction of target’s silicates in the upper layer mantle ( $r > R$ ) is denoted as  $F_{U,\text{tar}}$ . Runs with  $M_M > 1.0M_L$  and  $M_{\text{Fe}}/M_D < 0.1$  are regarded as successful impacts and denoted with bold (Ćuk & Stewart 2012). We note that most of the successful impacts also require special mechanisms to reduce the angular momentum (Wisdom & Tian 2015), although the degree of angular momentum reduction is lower than in the high angular momentum cases of Ćuk & Stewart (2012).

state (Canup et al. 2013; Figure 2). We calculate the entropy profile by arithmetically averaging the entropy across spherical shells (assuming spherical symmetry). The fraction of materials from the target is calculated analogously. The iron core is slightly oblate with an equatorial radius that is slightly (<5%) larger than the polar radius; hence, the assumption of spherical symmetry is a good assumption for characterizing the post-impact state even at the core-mantle boundary region. We summarize the results in Table 1.

Figure 3(c) shows the predicted fraction of target material in the post-impact body,  $F_{\text{tar}}$ , as a function of normalized enclosed mass (which corresponds to the radius, within which a given planetary mass fraction is enclosed). Even though mixing is more efficient with our new method than in previous studies, most of the impactor’s silicates still remain in the outer layer of the post-impact target mantle (low  $F_{\text{tar}}$ ). This prediction is explained by inefficient transfer of angular momentum during the impact (see Section 2). Focused shock heating in the outer layer results in a steep entropy profile (Figure 3(d)) through most of the mantle. In particular, there is a distinct entropy jump at radius  $R$ , or at a normalized enclosed mass of  $\sim 0.7 M_{\oplus}$ . In terms of mass, this  $R$  corresponds to  $\sim 1000$  km depth in the present-day mantle.

For the metal core, our models also predict a steep entropy and compositional profile in the aftermath of the impact. The entropy of the deep core even drops below its initial condition of  $1200 \text{ J kg}^{-1} \text{ K}^{-1}$ . This is well explained by the effects of phase transitions near the core-mantle boundary, which can be captured by the MFM method, and results in a redistribution of energy, and entropy, from the core to the mantle (Deng et al. 2019b; Figures 6, 7 and Section 6.1). The impactor’s metal mostly remains near the top of the core. Depending on the conditions of metal-silicate (impactor metallic core/target silicate mantle) equilibration, this prediction may provide an explanation for the  $\sim 300$  km thick compositionally stratified

layer that is seismically observed at the top of the present-day outer core (Helffrich & Kaneshima 2010).

#### 4. Geochemical Implications

To test our model predictions with geochemical observations, we estimate the unknown compositions of the impactor’s (Theia) and target’s (proto-Earth) mantles from the known isotopic compositions of the accessible part of the Earth’s mantle and Moon. In the following, these letters/subscripts denote material derived from the respective reservoirs: P = Proto-Earth, E = Earth (bulk), T = Theia (the impactor), U = Earth’s Upper Layer Mantle, L = Earth’s Lower Layer Mantle, M = Moon (bulk), or the Moon-forming disk, J = Ejecta (leaving the Earth–Moon system). Also,  $X$  is the isotopic composition of a reservoir (e.g., expressed in per mill deviation from a standard),  $m$  the mass of a reservoir, and  $f$  the fractional mass of the target (=the proto-Earth in Giant Impact settings) mantle in the reservoir.

All equations below will use the basic mass-balance equation, where two reservoirs of mass  $m_1$  and  $m_2$ , and isotopic compositions of  $X_1$  and  $X_2$ , are merged into a new reservoir of mass  $m_t = m_1 + m_2$  and composition  $X_t$ .  $X_t$  is then

$$X_t = [m_1 X_1 + m_2 X_2] / m_t. \quad (1)$$

Note that this assumes that the mass-fractions of the respective element (e.g., oxygen) are identical in all reservoirs. If that is not the case (e.g., if the proto-Earth’s mantle contains 40% O, while Theia’s mantle contains 45% O), then in the following,  $X_i$  should be treated as the product of the mass fraction  $c_i$  (e.g., 40%) and the actual isotopic composition  $X_i'$ :  $X_i = c_i X_i'$ . We start with the assumption that both the proto-Earth and Theia are initially well-mixed, so that their silicate mantles can be

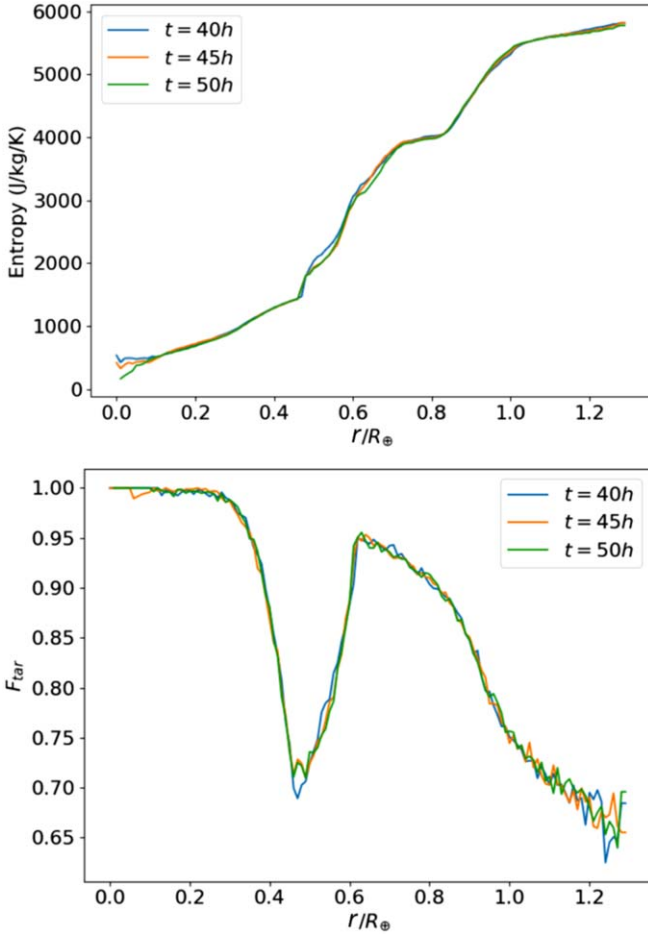


**Figure 2.** The thermal and compositional state of the post-impact target. The upper and lower panels display the entropy and compositional profiles, respectively, at different model times for run 13. After 40 hr, the post-impact target already has reached a stable state. This result confirms that our approach of performing the analysis at  $\geq 40$  hr after the impact is reliable.

treated as a single reservoir. In classical giant impact mass-balance calculations, one would fully mix these two reservoirs, with the respective contributions  $f_E$ ,  $f_M$  determined previously by the MFM simulations, to arrive at the resulting bulk isotopic composition of Earth and Moon. The mass-balance calculation for the isotopic composition of (the silicate part of) the Earth is

$$X_E = [m_{P,E}X_P + m_{T,E}X_T]/m_E. \quad (2)$$

So,  $m_{P,E}$  is the total mass of the proto-Earth mantle material that ends up in the Earth’s mantle, while  $m_E$  is the mass of the Earth’s mantle. For convenience, we can also define

$$f_i = m_{P,i}/m_i, \quad (3)$$

so that  $f_i$  is the fraction of proto-Earth mantle material in the respective reservoir ( $i$ ). Since the rest of the mass of the reservoir must come from Theia ( $m_{P,i} + m_{T,i} = m_i$ ) we can also set

$$m_{T,i} = (1 - f_i)m_i. \quad (4)$$

We can then re-write Equation (2) as

$$X_E = f_E X_P + (1 - f_E)X_T. \quad (5)$$

Similarly, we can formulate the same equation for the Moon,

$$X_M = f_M X_P + (1 - f_M)X_T. \quad (6)$$

Here,  $f_M$  represents the fraction of proto-Earth mantle material in the Moon. The fact that  $f_E$  and  $f_M$  (and thus  $X_E$  and  $X_M$ ; all other values must be the same) have been found to be different in MFM simulations of the giant impact, while  $X_E$  and  $X_M$  have been measured to be identical within uncertainty, is sometimes called the “isotopic conundrum” of the Moon’s formation (Asphaug 2014). In the paper, we show that a giant impact simulated with an updated MFM model will result in a stratified Earth mantle, where the upper mantle contains a smaller fraction of proto-Earth material than the lower mantle, although the proto-Earth fractions of the upper mantle and the disk (from which the Moon forms) are similar. The composition of the three reservoirs is then

$$X_M = [m_{P,M}X_P + m_{T,M}X_T]/m_M, \quad (7)$$

$$X_U = [m_{P,U}X_P + m_{T,U}X_T]/m_U, \quad (8)$$

$$X_L = [m_{P,L}X_P + m_{T,L}X_T]/m_L. \quad (9)$$

There is a fourth reservoir, which contains ejecta, material ejected from the Earth–Moon-system back into a heliocentric orbit. For canonical impacts, this reservoir has masses between 0.001 and 0.02 Earth masses, while for hit-and-run impacts, the masses are considerably larger, between 0.04 and 0.07 Earth masses. For simplicity, we will assume that for canonical impacts, the contribution from the proto-Earth is zero, while for hit-and-run impacts, the proto-Earth contribution is typically on the order of 30%. The mass-balance equation for the ejecta reservoir is

$$X_J = [m_{P,J}X_P + m_{T,J}X_T]/m_J. \quad (10)$$

As for the “simple” case of the fully mixed post-giant-impact Earth (Equations (5) and (6)), we can again express the  $m_{P,i}$  and  $m_{T,i}$  variables using the respective contribution from the proto-Earth:

$$X_M = f_M X_P + (1 - f_M)X_T \quad (11)$$

$$X_U = f_U X_P + (1 - f_U)X_T \quad (12)$$

$$X_L = f_L X_P + (1 - f_L)X_T \quad (13)$$

$$X_J = f_J X_P + (1 - f_J)X_T. \quad (14)$$

Since we have constraints for the isotopic composition of the Moon ( $X_M$ ) and the upper mantle ( $X_U$ ) as well as the masses and/or proto-Earth contributions in all reservoirs (from the MFM simulations;  $m_i$  and/or  $f_i$ ), we are left with four unknown variables ( $X_P$ ,  $X_T$ ,  $X_L$ ,  $X_J$ ) and four equations relating them. We use Equations (11) and (12) to solve for  $X_P$  and  $X_T$ , which are then in turn used to calculate  $X_L$  and  $X_J$  using (13) and (14).

$$X_T = [f_U X_M - f_M X_U]/[f_U(1 - f_M) - f_M(1 - f_U)] \quad (15)$$

$$X_P = [X_M - (1 - f_M)X_T]/f_M. \quad (16)$$

The above isotope composition calculation based on mass balance is universal for all elements. Here we use the data for  $\Delta^{17}\text{O}$  because it is measured with high precision and used as a tracer in  $N$ -body simulations (Mastrobuono-Battisti & Perets 2017).



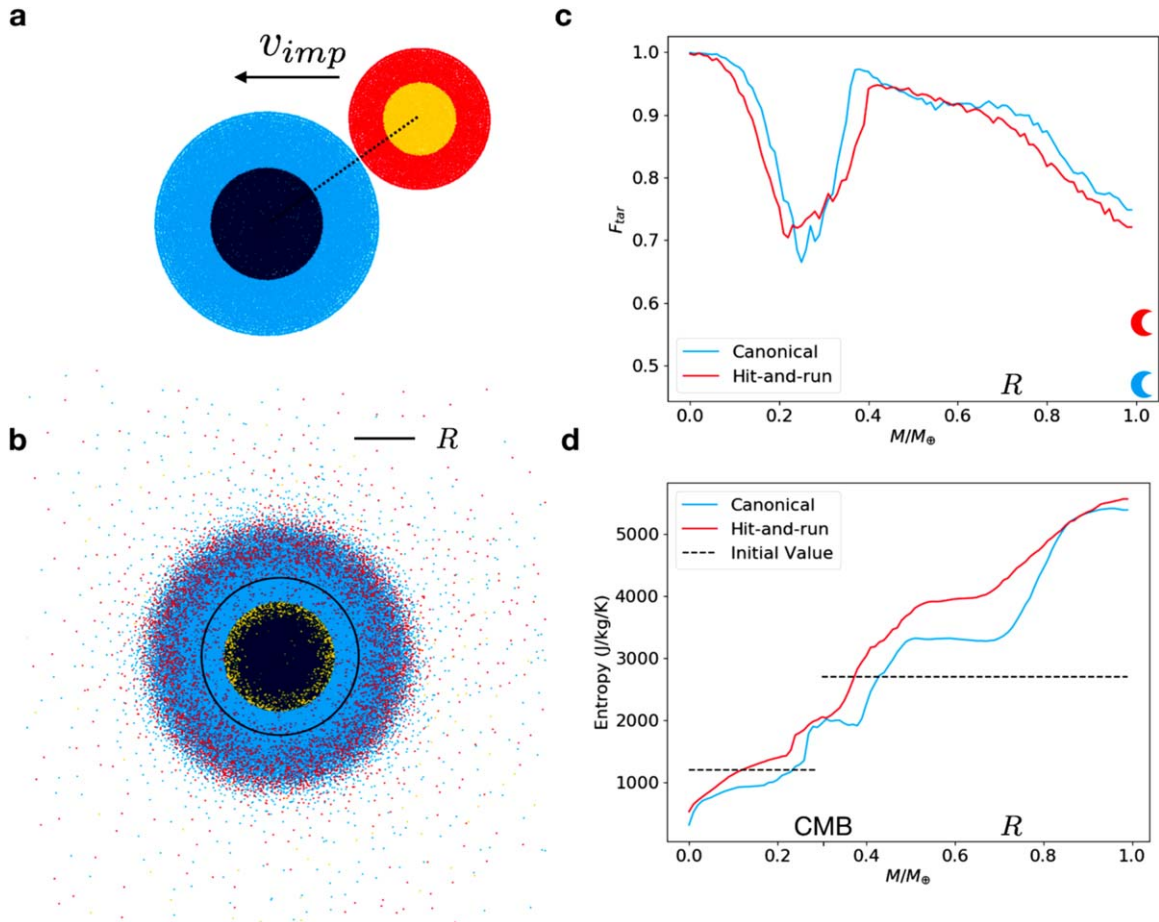


**Figure 3.** The internal structure of the post-impact Earth, after canonical (e.g., run 5) and hit-and-run collisions (e.g., run 13). (a) The initial condition just before the impact with the impactor’s and target’s mantle/core as marked with red/yellow and light-blue/dark-blue colors, respectively. The compositional structure of the post-impact target is visualized as (b) a 2D cross-section through the 3D model for run 13, and (c) 1D average profiles for runs 5 (canonical, blue) and 13 (hit-and-run, red). The average composition of the disk is denoted by a crescent Moon symbol. (d) shows the related entropy profiles with black dash lines indicating the initial condition. A significant entropy jump is predicted at a radius  $R$  (i.e., at a normalized enclosed mass of  $\sim 0.7M_{\oplus}$ ), corresponding to a kink in the compositional profile (see also (b), inside radius  $R$  there are more blue points).

Figure 4(a) shows the allowed  $\Delta^{17}\text{O}$ -difference as a function of the mass of the mantle that remains poorly homogenized (or preserved) over the age of the Earth. The stated uncertainties of the isotopic compositions of the different reservoirs (e.g., Theia, proto-Earth, etc.) are estimated by using the maximal difference in O isotopic composition (Herwartz et al. 2014) allowed between the Earth ( $\Delta^{17}\text{O} = -0.101 \pm 0.002\text{‰}$ ) and Moon ( $-0.089 \pm 0.002\text{‰}$ ) within the respective uncertainties, i.e.,  $-0.103\text{‰}$  for the Earth and  $-0.087\text{‰}$  for the Moon, and then determining the difference to the nominal value. This conservative approach tends to overestimate the uncertainties. If the present-day mantle is fully homogenized such that any primordial stratification is completely removed, a common assumption in previous studies, Theia and the proto-Earth must have been rather similar in composition. For example, only 30 ppm  $\Delta^{17}\text{O}$  difference between parent bodies are allowed in our best canonical model (run 5). On the other hand, if the assumption of full homogenization is relaxed, and the predicted mantle stratification can be (partially) preserved through the present day, larger compositional differences can be reconciled with the available data. For example, considering the preservation of a compositionally distinct domain below  $R$ ,

differences of up to 54 ppm (run 13) in  $\Delta^{17}\text{O}$  are allowed (Figure 4(b)), particularly for the hit-and-run models, which display larger fractions of proto-Earth silicate material in the disk than the canonical models (Table 1; Figure 3). These large values are consistent with the compositional difference between potential parent bodies of the Earth–Moon system in  $N$ -body simulations of planetary accretion (Mastrobuono-Battisti & Perets 2017). For realistic parent-body compositional differences (Dauphas 2017), inefficient mixing of the Earth’s mantle through time can indeed help to resolve the geochemical similarity of the accessible Earth mantle and Moon. Even for moderate mixing across  $R$ , our models can critically increase the allowed compositional difference between parent bodies (see Figure 4(a)). As a consequence, the likelihood of potential parent pairs, which is a steep function of the compositional difference (Mastrobuono-Battisti & Perets 2017), increases significantly.

As a cautionary note, recent oxygen isotope measurements found smaller  $\Delta^{17}\text{O}$  difference between the Moon and the accessible mantle (Young et al. 2016; Greenwood et al. 2018). The same run 13, using instead the Earth and Moon  $\Delta^{17}\text{O}$  values from Greenwood et al. (2018) that imply that the Earth

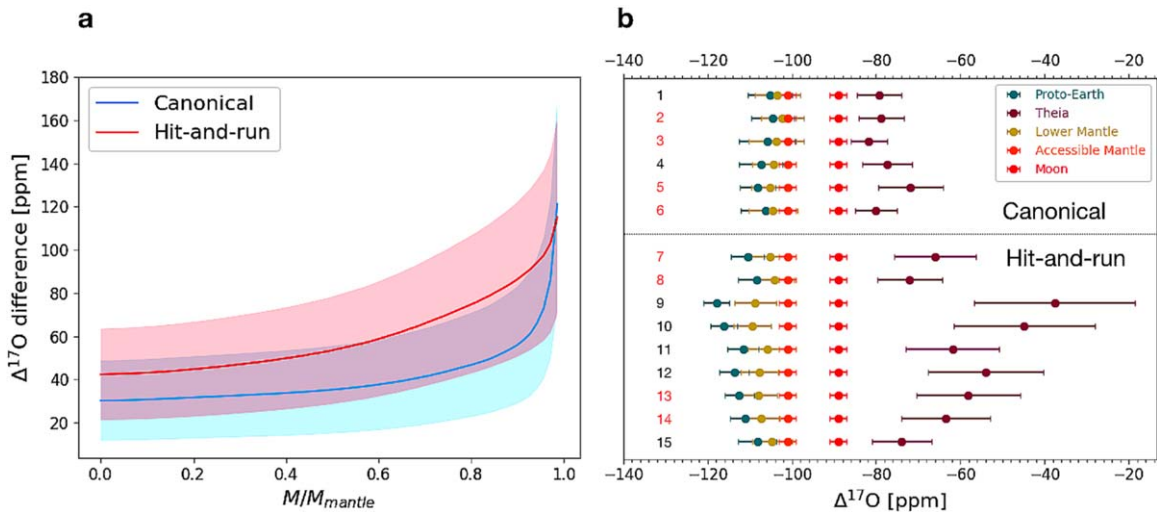


**Figure 4.** Oxygen isotopic composition of all reservoirs involved in the collision. Using the compositional profiles predicted by our models, we calculate the compositions of the lower-mantle layer, Theia, and proto-Earth based on those of the accessible present-day mantle and Moon (Herwartz et al. 2014). Panel (a) shows the allowed  $\Delta^{17}\text{O}$  difference between Theia and the proto-Earth for runs 5 (blue) and 13 (red) as a function of the mass of the reservoir that remains unmixed with the accessible mantle. The shaded regions/error bars correspond to  $1\sigma$  SEM uncertainty (Herwartz et al. 2014). Panel (b) shows the estimated  $\Delta^{17}\text{O}$  for all reservoirs and all runs (Table 1) assuming that no mixing occurs in the Earth’s mantle across  $R$  (i.e., mass of the unmixed reservoir is  $\sim 50\%$  of that of the mantle). For example, Theia’s oxygen isotopic composition could have been up to 54 ppm higher than that of the proto-Earth for run 13, simultaneously resulting in an isotopic difference between the accessible and lower mantle of 7 ppm.

and Moon differ by only about 4 ppm, allows only  $<20$  ppm difference between Theia and the proto-Earth. This difference (54 ppm versus 20 ppm) corresponds to a very big difference in likelihood of the needed Theia-proto-Earth in (Mastrobuono-Battisti & Perets 2017).

### 5. Preservation of Heterogeneity

Whether post-impact heterogeneity can persist through  $\sim 1$  Myr of magma ocean and  $\sim 4.5$  Gyr of mantle, convection is controlled by the initial thermal profile, and in particular, the initial compositional profile of the mantle. Our models predict the formation of a deep magma ocean due to the energy release of the giant impact (Nakajima & Stevenson 2015). While major-element compositions of the post-impact mantle layers above and below  $R$  depend on the unknown bulk compositions of Theia and the proto-Earth, respectively, an enrichment of the lower (proto-Earth) layer in FeO and  $\text{SiO}_2$  is generally consistent with the evolving physical conditions (temperatures, pressures, oxidation state) of core formation during progressive planetary accretion (Kaminski & Javoy 2013; Rubie et al. 2015; Wade & Wood 2016). Furthermore, FeO-enrichment of the deep proto-Earth’s mantle may have been generated by compositional fractionation (and subsequent overturn; Elkins-Tanton 2008) during any magma-ocean episode(s) that predate(s) the Moon-forming impact. Even just a slight FeO-enrichment of the lower layer is sufficient to promote stable stratification through various magma-ocean stages. While stable layering is further promoted by the entropy gradient across the post-impact mantle (i.e., sub-adiabatic temperature profile) as predicted by our models, thermal stratification should be removed during cooling of the magma ocean (Nakajima & Stevenson 2015).

After the final magma-ocean episode that follows the giant impact, mixing during long-term solid-state mantle convection is controlled by the density and viscosity contrasts between the two layers. Any enrichment of the proto-Earth’s mantle in FeO and/or  $\text{SiO}_2$  (see above) is expected to impede efficient mixing

of the mantle by sustaining intrinsically high densities and viscosities, respectively. Thereby, a significant enrichment in FeO can promote double-layered convection with limited mass exchange between layers (Kellogg et al. 1999; Tosi et al. 2013). In turn, an enrichment of the lower layer in  $\text{SiO}_2$  can promote the survival of intrinsically strong primordial heterogeneity as blobs with a wide range of spatial scales (meters to 1000 s kilometers) that are poorly mixed and entrained even by single-layered convection (Manga 1996; Ballmer et al. 2017). For example, Kaminski & Javoy (2013) predict a molar Mg/Si of  $\sim 0.98$  for the proto-Earth’s (lower) mantle, corresponding to the predominant abundance of the high-viscosity mineral bridgmanite  $(\text{Mg,Fe})\text{SiO}_3$ , which may stabilize large unmixed blobs (Ballmer et al. 2017). Finally, for no enrichment or even depletion in FeO and  $\text{SiO}_2$ , no significant preservation of heterogeneity that pre-dates the Moon-forming giant impact is expected.

In contrast, geophysical and geochemical evidence attest to a limited degree of mantle mixing, hence lending further support to an enrichment in FeO and/or  $\text{SiO}_2$  of the proto-Earth’s mantle relative to the impactor’s mantle. While some degree of whole-mantle mixing is indicated by the sinking of a subset of subducted slabs of oceanic lithosphere through the entire mantle, the stagnation of other slab segments (Fukao & Obayashi 2013) and the deflection of upwelling plumes (French & Romanowicz 2015) at  $\sim 1000$  km depth (i.e., about radius  $R$ ) is indeed consistent with restricted mixing. Sharp seismic-velocity contrasts at similar depths support this interpretation, and provide direct evidence for large-scale compositional mantle heterogeneity (Jenkins et al. 2017; Waszek et al. 2018). The preservation of primordial noble gases (Mukhopadhyay 2012), e.g., the large missing budget of argon (Allègre et al. 1996) provides complementary evidence for heterogeneous accretion and incomplete homogenization of primordial mantle reservoirs. In turn, no resolvable anomaly in oxygen isotopic space is found in igneous mantle rocks with a putative deep-mantle or plume origin (Starkey et al. 2016).

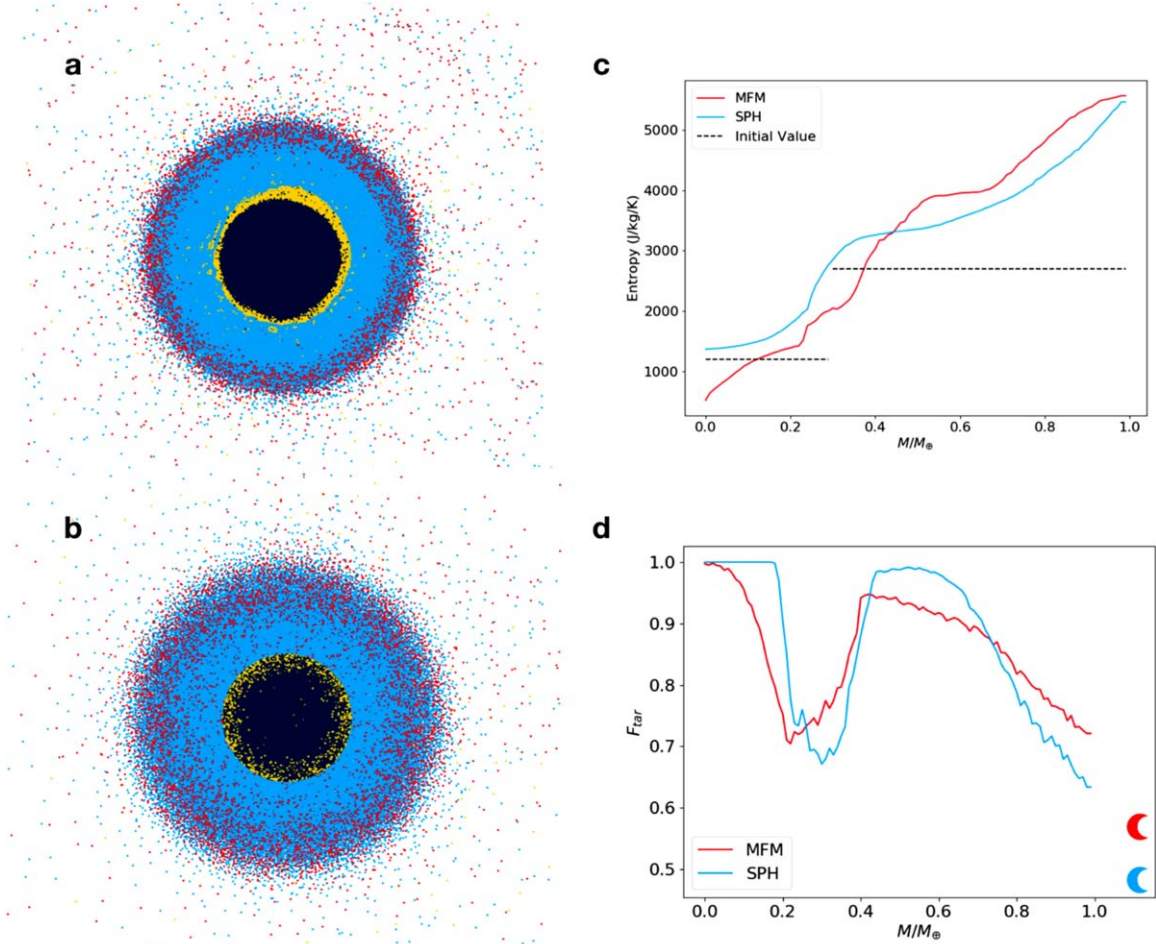


**Figure 5.** Comparison between MFM and standard SPH simulation of run 13 in Table 1. (a) and (b) show the material distribution in the post-impact target in the SPH and MFM run, respectively. Compared to MFM, impactor materials tend to be enhanced near the planet’s surface and near to top of the core in SPH, and nearly absent in the deep mantle and core (Deng et al. 2019b). (c) The entropy profile for both methods. The entropy jump in the mantle is sharper for MFM than for SPH. In the MFM simulations, the entropy drop in the core is explained by transfer of energy due to the phase transition at the core-mantle boundary (Deng et al. 2019b; Figure 6). (d) The mass fraction of materials from the target is plotted as a function of the normalized enclosed mass. Mixing of impactor material with the deep target mantle and core is more efficient for MFM than for SPH. For a detailed discussion in terms of the comparison of both approaches, we refer the reader to Deng et al. (2019b).

Note, however, that plumes mostly entrain recycled components (Hofmann 1997), and any primordial signatures may be diluted below analytical precision for oxygen isotopic anomalies that are small to start with (Figure 4). In contrast,  $^{182}\text{W}$  isotopic anomalies across the solar system are larger than those of oxygen relative to analytical precision, hence being a more suitable tracer of primordial heterogeneity in the Earth’s mantle. Indeed,  $^{182}\text{W}$  evidence (Rizo et al. 2016; Mundl et al. 2017) requires that at least a subset of the preserved ancient reservoir evident by noble-gas systematics pre-dates the Moon-forming impact (Barboni et al. 2017), and thus reflects proto-Earth compositions. In any case, additional constraints on the present-day structure of the mantle are needed to further bracket the compositions of the proto-Earth, and Theia.

## 6. Numerical Issues and Robustness

We compare MFM simulations with traditional SPH simulations and examine the robustness of our MFM predictions with respect to simulation resolution and initial entropy in this section. We stress again that the code we use here, GIZMO (Hopkins 2017), is a multi-method code, including both

SPH and MFM. In this framework MFM and SPH share the same EOS implementation; so the difference found between these two numerical methods in the manuscript, especially in terms of the entropy difference, can only be caused by differences in the hydrodynamical method. There are two major differences between the two methods that are relevant for our discussion. First, traditional SPH suffers from spurious pressure forces at contact discontinuities (Agertz et al. 2007). In impact simulations, these forces may separate the core and mantle to some extent regardless of the resolution (see. e.g., Kegerreis et al. 2019). We note that modern SPH (see e.g., GASOLINE2 in Reinhardt et al. 2019) can handle the core-mantle boundary faithfully. Second, SPH imposes artificial viscosity to capture shocks, which can result in excessive dissipation and suppress subsonic turbulence (for our case affecting mixing in the post-impact body; see, e.g., Bauer & Springel 2012). MFM is a relatively new method that does not suffer from the above two shortcomings, as recently shown in published papers describing the GIZMO code. For example, we note that MFM successfully passes benchmark tests such as the Kelvin–Helmholtz instability and forced subsonic turbulence test (Hopkins 2015),



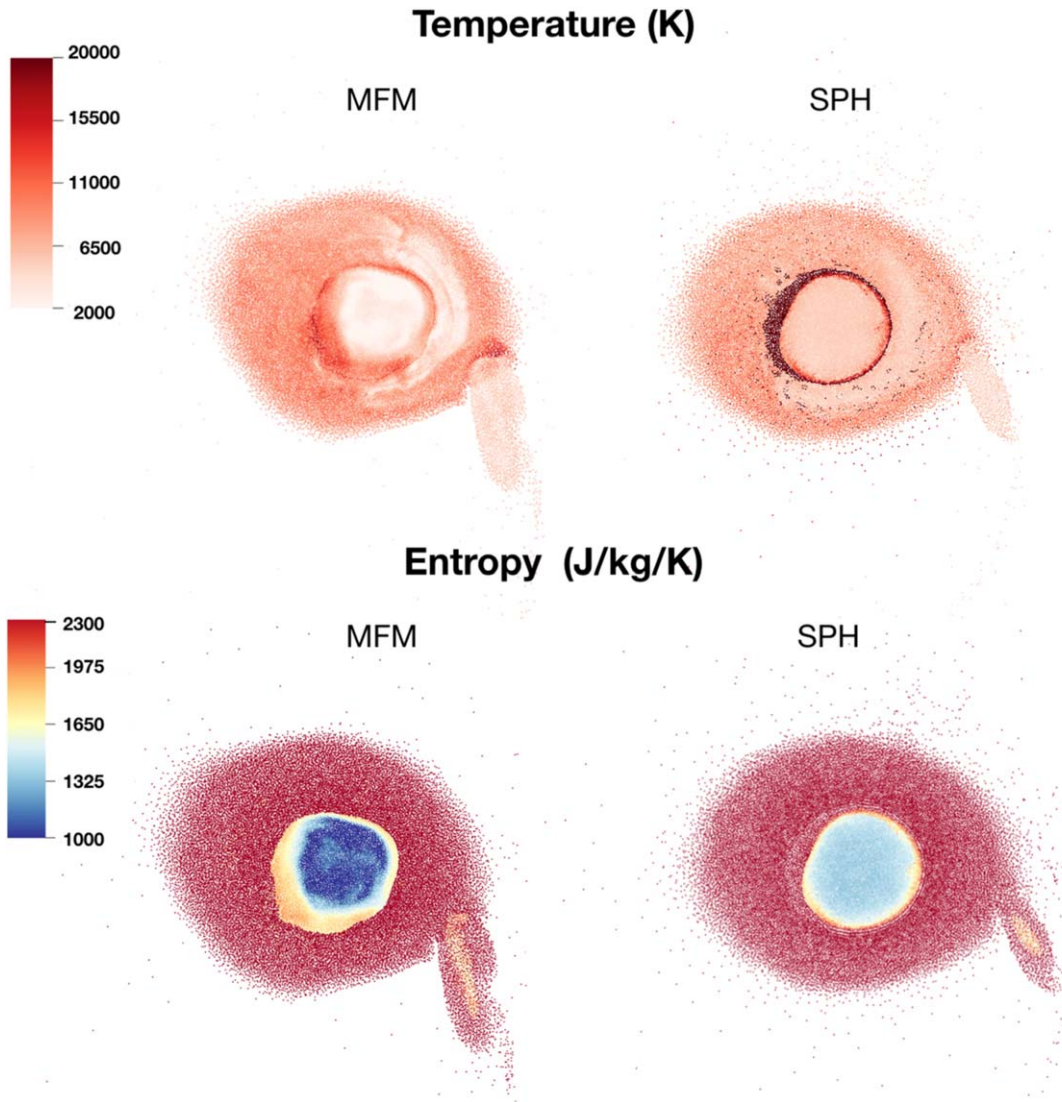


**Figure 6.** Difference of the thermal state in MFM and SPH simulations of run 13 (hit-and-run). We show snapshots of the SPH and MFM comparison run at 7.08 hr. There is a clear separation between the core and mantle in the SPH simulation due to numeric issues (Deng et al. 2019b); the temperature difference across the core-mantle boundary can be larger than 10,000 K (see also Reufer et al. 2012).

which deal exactly with the two shortcomings described above. These capabilities of MFM are inherited from the fact that it solves the hydro equations in conservative form using an accurate Riemann solver and employing all the machinery of state-of-the-art finite volume 2nd order Godunov codes.

### 6.1. Comparison with SPH

The entropy structures in our MFM models contrast with that of our SPH models (Figure 5). The entropy drop in the core for MFM is caused by a phase transition and the associated redistribution of internal energy, and entropy, from the core to the mantle, hence it has a physical origin (Deng et al. 2019b). Indeed, as the outer core, near the core-mantle boundary, melts first, entropy locally increases, forcing the inner core to decrease its own entropy in order to maintain thermodynamical equilibrium (see Appendix). This entropy loss outweighs the entropy gain through shocks in the central core region. In contrast, in SPH simulations, the core and mantle are separated

by an artificial tensional force (Agertz et al. 2007; Hosono et al. 2016; Deng et al. 2019b; see also Figure 6). This force largely isolates the core, causing the core to evolve nearly adiabatically (Deng et al. 2019b). The physical heating associated with shocks is somewhat overestimated by the usage of artificial viscosity (Springel 2005; Deng et al. 2019b); as a result, the entropy slightly increases in the core for SPH. That the entropy in the central core does not decrease for SPH, is thus mostly due to a numerical artifact. Results obtained by MFM also display a sharper entropy jump in the mantle than those obtained by SPH, because MFM allows for sharper capturing of shocks (Hopkins 2015). The marked difference between MFM and SPH, i.e., in terms of the temperature and entropy distribution near the core-mantle boundary, is visualized in Figure 6. Regarding the compositional profile of Figure 5, SPH shows abrupt boundary between the impactor’s and target’s materials due to numerical suppression of mixing (Deng et al. 2019b).



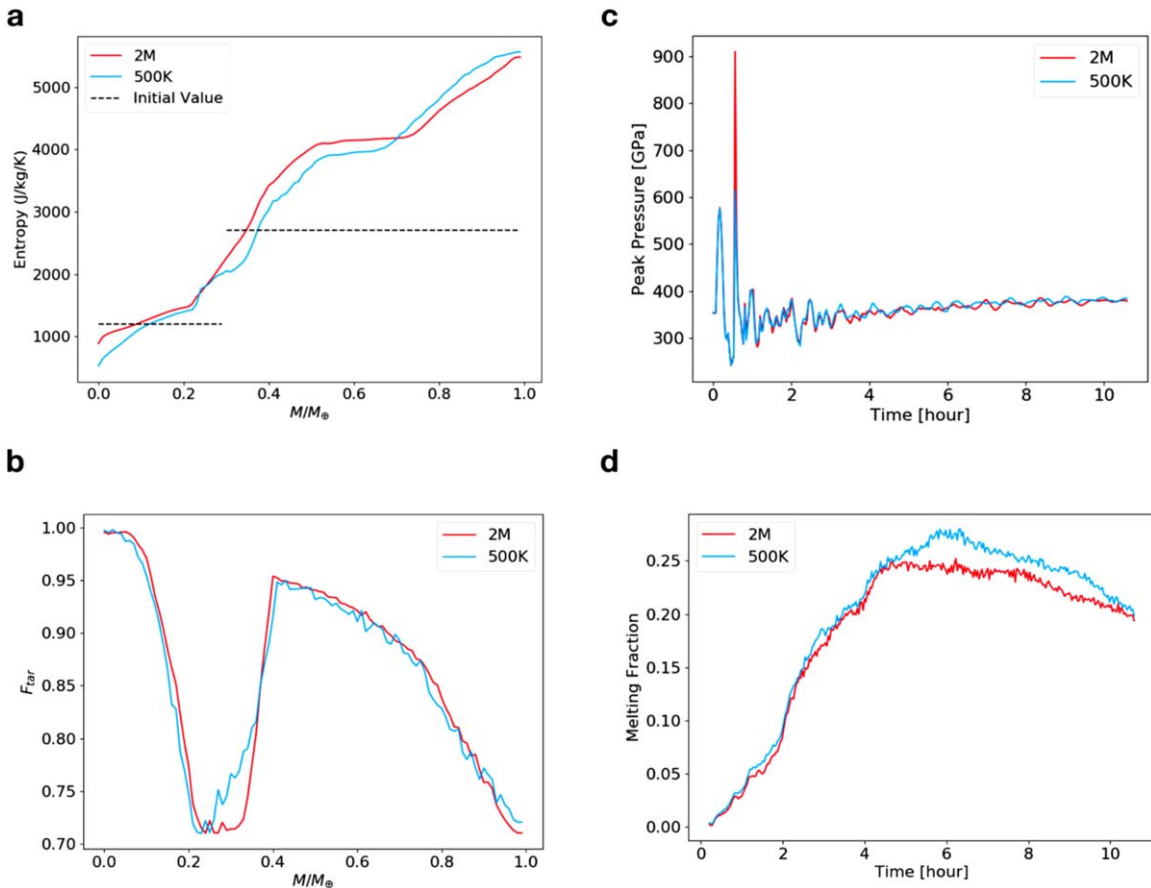


**Figure 7.** Resolution test of our MFM simulations in terms of number of particles. A high-resolution case with 2M particles (and otherwise the same parameters as run 13) indeed numerically converges well with run 13. Even though small differences persist in terms of the details of the (a) entropy profile, (c) peak pressure, and (d) melt fraction of the core (Pierazzo et al. 1997), the most critical model prediction (i.e., (b) the compositional profile) converges well at the two resolutions shown. The pressure fluctuation is stronger in the lower resolution simulation (due to larger discretization noise), which leads to exaggerated melt fraction in the core.

## 6.2. Robustness of Radial Structure

We run a 2M particle simulation as a convergence test (see Figure 7) and a simulation with higher initial entropy to check the effects of the initial thermal state on the post-impact target (see Figure 8). We acknowledge that achieving a quantitatively converged thermal state in general, and for the energy flux in particular, is challenging, and will likely require higher resolution than used here (not possible for a parameter study), because low resolution leads to strong oscillations (poor force resolution), more melting and more energy extraction from the core (Figure 7). We stress, however, that our conclusions remain robust as the compositional profile remains virtually unaffected by changes in resolution (Figure 7) or in the initial thermal state (Figure 8). While these changes affect the entropy profile (see above), they do not affect the compositional profile. Future studies with DISPH (Hosono et al. 2016), GDSPH (see tests in Reinhardt et al. 2019), or CRKSPH (Frontiere et al. 2017) using the ANEOS library will shed further light on the entropy drop in the center core. We expect DISPH to be in line with MFM as in the ideal gas simulations (Saitoh & Makino 2016). The cooling core may also be a pure artifact caused by the treatment of phase transitions in ANEOS which may not be that realistic (K. Wünnemann, private communication). Indeed there are ongoing projects on improving the

accuracy of the ANEOS equation of state library (see, e.g., Stewart et al. 2019). In all, reevaluation of the reliability/accuracy of giant impact modeling deserves more attention.

## 7. Conclusions

We carried out hydrodynamical simulations for low energy Moon-forming impacts. We focused on the structure of the post-impact proto-Earth. Due to inefficient angular momentum transport, the post-impact proto-Earth forms two layers. The hot upper layer is compositionally similar to the proto-lunar disk while the lower layer is mainly composed of the pre-impact target’s material. If the upper layer remains poorly mixed with the lower layer, the degree of isotope similarity measured between the accessible mantle (upper layer) and Moon occurs in half of the potential Moon-forming impacts in  $N$ -body simulations of Mastrobuono-Battisti & Perets (2017). Preservation of  $\text{SiO}_2$ -enriched heterogeneity further helps to balance the bulk-Earth’s silica budget relative to the chondritic reservoir. Future geochemical and geophysical studies of lower-mantle composition will contribute to constrain the chemistry and origin of Earth’s parent bodies, and thus, ultimately, of the inner solar nebula.

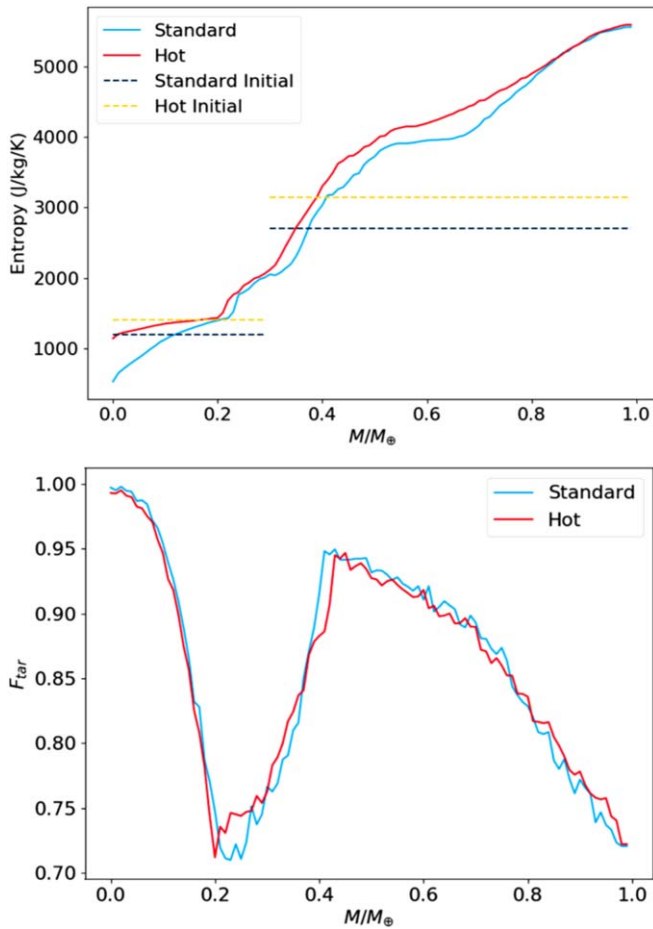


**Figure 8.** Model results as a function of initial condition. The upper and lower panels shows the final entropy and compositional profiles, respectively, for run 13 (blue), and an analogous case with a higher initial entropy target ( $1400 \text{ J kg}^{-1} \text{ K}^{-1}$  for iron and  $3200 \text{ J kg}^{-1} \text{ K}^{-1}$  for dunite) for iron and dunite (red). In the case with an initially hotter target, the entropy jump in the mantle is slightly less sharp than for run 13. However, the compositional profile is robust, remaining virtually unchanged. The disk mass and angular momentum also remain robust with differences  $<2\%$ .

We thank Romain Teyssier and Martin Jutzi for useful discussions. We are grateful to the referees, Kaveh Pahlevan, and the other anonymous referee for comments that help to improve the manuscript a lot. We acknowledge support from the Swiss National Science Foundation via the NCCR PlanetS.

*Software:* GIZMO code (Hopkins 2015), ballistic (Reinhardt & Stadel 2017).

## Appendix Phase Diagram of the Target's Core

In Figure 9, we plot the phase diagram of the target's core in run 13 (Table 1) to show how the outer core melts and transfer internal energy from the inner core outwards. Initially, the core is solid (below the red curve, i.e., the iron solidus) with an entropy about  $1200 \text{ J kg}^{-1} \text{ K}^{-1}$ . Without any perturbation, the core of such an isolated target retains this state for  $>40$  hr (the giant impact simulation timescale). At 0.35 hr, the primary shock just passes through the target heating the core to higher entropy. At the same time, pressure unloading of the target leads to expansion of the core (Asphaug et al. 2006). These two effects combined result in a partial molten outer core (Figure 9 middle panel, regions with density smaller than  $12 \text{ g cm}^{-3}$ ). The target experiences strong oscillations before it settles down (see Figure 7). During subsequent compression (e.g., at 2.48 hr), internal energy flows from solid to melts to achieve quasi-pressure equilibrium because melts have high internal energy compared to solids at the same pressure. Further expansion produces more melts in the outer core. These oscillation cycles result in the hot outer core in Figure 6 in both MFM and SPH simulations. MFM can further transfer the gained internal energy from the inner core to the mantle while SPH cannot due to the numerical core-mantle separation leading to a temperature difference  $>10,000 \text{ K}$  across the core-mantle boundary.

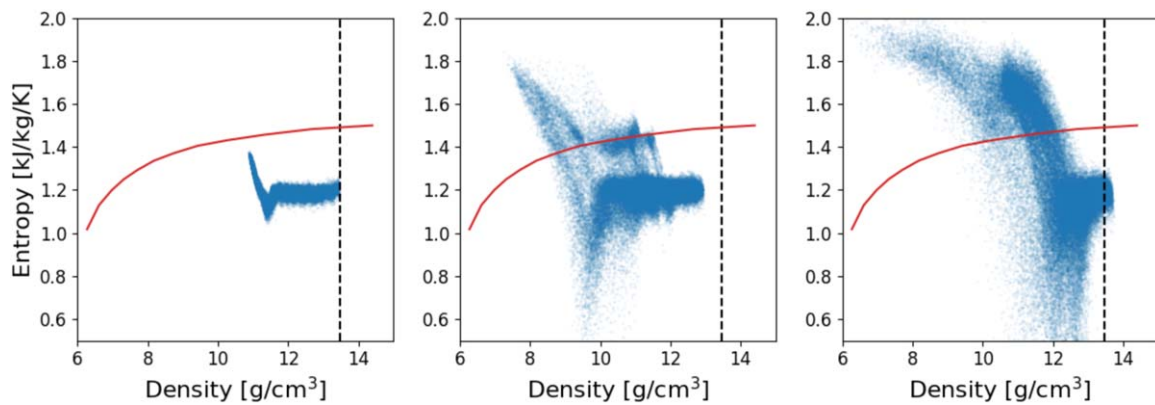


**Figure 9.** The phase diagram (entropy vs. density scatter plot) of the target's core in run 13 at  $t = 0, 0.35,$  and  $2.48$  hr from left to right. The red curves show the iron solidus. The vertical dash lines indicate the maximum density at  $t = 0$ .

### ORCID iDs

Hongping Deng  <https://orcid.org/0000-0001-6858-1006>

### References

- Agertz, O., Moore, B., Stadel, J., et al. 2007, *MNRAS*, **380**, 963  
Allègre, C. J., Hofmann, A., & O'Nions, K. 1996, *GeoRL*, **23**, 3555  
Asphaug, E. 2014, *AREPS*, **42**, 551  
Asphaug, E., Agnor, C. B., & Williams, Q. 2006, *Natur*, **439**, 155  
Ballmer, M. D., Houser, C., Hernlund, J. W., Wentzcovitch, R. M., & Hirose, K. 2017, *NatGe*, **10**, 236  
Barboni, M., Boehnke, P., Keller, B., et al. 2017, *SciA*, **3**, e1602365  
Bauer, A., & Springel, V. 2012, *MNRAS*, **423**, 2558  
Cameron, A. G., & Ward, W. R. 1976, *LPSC*, **7**, 120  
Canup, R. M. 2012, *Sci*, **338**, 1052  
Canup, R. M., & Asphaug, E. 2001, *Natur*, **412**, 708  
Canup, R. M., Barr, A. C., & Crawford, D. A. 2013, *Icar*, **222**, 200  
Čuk, M., & Stewart, S. T. 2012, *Sci*, **338**, 1047  
Dauphas, N. 2017, *Natur*, **541**, 521  
Deng, H., Mayer, L., Latter, H., Hopkins, P. F., & Bai, X.-N. 2019a, *ApJS*, **241**, 26  
Deng, H., Mayer, L., & Meru, F. 2017, *ApJ*, **847**, 43  
Deng, H., Reinhardt, C., Benitez, F., et al. 2019b, *ApJ*, **870**, 127  
Elkins-Tanton, L. T. 2008, *E&PSL*, **271**, 181  
French, S. W., & Romanowicz, B. 2015, *Natur*, **525**, 95  
Frontiere, N., Raskin, C. D., & Owen, J. M. 2017, *JCoPh*, **332**, 160  
Fukao, Y., & Obayashi, M. 2013, *JGRB*, **118**, 5920  
Greenwood, R. C., Barrat, J.-A., Miller, M. F., et al. 2018, *SciA*, **4**, eaao5928  
Hartmann, W. K., & Davis, D. R. 1975, *Icar*, **24**, 504  
Helffrich, G., & Kaneshima, S. 2010, *Natur*, **468**, 807  
Herwartz, D., Pack, A., Friedrichs, B., & Bischoff, A. 2014, *Sci*, **344**, 1146  
Hofmann, A. W. 1997, *Natur*, **385**, 219  
Hopkins, P. F. 2015, *MNRAS*, **450**, 53  
Hopkins, P. F. 2017, arXiv:1712.01294  
Hosono, N., Iwasawa, M., Tanikawa, A., et al. 2017, *PASJ*, **69**, 26  
Hosono, N., Karato, S.-i., Makino, J., & Saitoh, T. R. 2019, *NatGe*, **12**, 418  
Hosono, N., Saitoh, T. R., Makino, J., Genda, H., & Ida, S. 2016, *Icar*, **271**, 131  
Jackson, A. P., Gabriel, T. S., & Asphaug, E. I. 2017, *MNRAS*, **474**, 2924  
Jenkins, J., Deuss, A., & Cottaar, S. 2017, *E&PSL*, **459**, 196  
Kaminski, E., & Javoy, M. 2013, *E&PSL*, **365**, 97  
Karato, S.-I. 2014, *PJAB*, **90**, 97  
Kegerreis, J. A., Eke, V. R., Gonnet, P., et al. 2019, *MNRAS*, **487**, 5029  
Kellogg, L. H., Hager, B. H., & Van Der Hilst, R. D. 1999, *Sci*, **283**, 1881  
Lock, S. J., & Stewart, S. T. 2017, *JGRE*, **122**, 950  
Lock, S. J., Stewart, S. T., Petaev, M. I., et al. 2018, *JGRE*, **123**, 910  
Manga, M. 1996, *GeoRL*, **23**, 403  
Mastrobuono-Battisti, A., & Perets, H. B. 2017, *MNRAS*, **469**, 3597  
Melosh, H. 2007, *M&PS*, **42**, 2079  
Mukhopadhyay, S. 2012, *Natur*, **486**, 101  
Mundt, A., Touboul, M., Jackson, M. G., et al. 2017, *Sci*, **356**, 66  
Nakajima, M., & Stevenson, D. J. 2015, *E&PSL*, **427**, 286  
Pahlevan, K., & Morbidelli, A. 2015, *Natur*, **527**, 492  
Pahlevan, K., & Stevenson, D. J. 2007, *E&PSL*, **262**, 438  
Pierazzo, E., Vickery, A., & Melosh, H. 1997, *Icar*, **127**, 408  
Reinhardt, C., Chau, A., Stadel, J., & Helled, R. 2019, arXiv:1907.09809  
Reinhardt, C., & Stadel, J. 2017, *MNRAS*, **467**, 4252  
Reufer, A., Meier, M. M., Benz, W., & Wieler, R. 2012, *Icar*, **221**, 296  
Rizo, H., Walker, R. J., Carlson, R. W., et al. 2016, *Sci*, **352**, 809  
Rubie, D. C., Jacobson, S. A., Morbidelli, A., et al. 2015, *Icar*, **248**, 89  
Rufu, R., Aharonson, O., & Perets, H. B. 2017, *NatGe*, **10**, 89  
Saitoh, T. R., & Makino, J. 2016, *ApJ*, **823**, 144  
Springel, V. 2005, *MNRAS*, **364**, 1105  
Starkey, N. A., Jackson, C. R., Greenwood, R. C., et al. 2016, *GeCoA*, **176**, 227  
Stewart, S. T., Davies, E. J., Duncan, M. S., et al. 2019, arXiv:1910.04687  
Thompson, S., & Lauson, H. 1974, Improvements in the Chart D Radiation-hydrodynamic CODE III: Revised Analytic Equations of State, Tech. Rep., No. SC-RR-71-0714  
Tosi, N., Plesa, A.-C., & Breuer, D. 2013, *JGRE*, **118**, 1512  
Wade, J., & Wood, B. J. 2016, *E&PSL*, **442**, 186  
Waszek, L., Schmerr, N. C., & Ballmer, M. D. 2018, *NatCo*, **9**, 385  
Wisdom, J., & Tian, Z. 2015, *Icar*, **256**, 138  
Young, E. D., Kohl, I. E., Warren, P. H., et al. 2016, *Sci*, **351**, 493  
Zhang, J., Dauphas, N., Davis, A. M., Leya, I., & Fedkin, A. 2012, *NatGe*, **5**, 251  
Zhu, Q., Hemquist, L., & Li, Y. 2015, *ApJ*, **800**, 6